ChemCatChem

Research Article
doi.org/10.1002/cctc.202200703

Chemistry Europe
European Chemical Societies Publishing

www.chemcatchem.org

Operando X-ray Powder Diffraction Study of Mechanochemical Activation Tested for the CO Oxidation over Au@Fe_2O_3 as Model Reaction

Hilke Petersen,[a] Jacopo De Bellis,[a] Sebastian Leiting,[a] Saurabh Mohan Das,[b] Wolfgang Schmidt,[a] Ferdi Schüth,[a] and Claudia Weidenthaler*[a]

Mechanochemistry has proven to be an excellent green synthesis method for preparing organic, pharmaceutical, and inorganic materials. Mechanocatalysis, inducing a catalytic reaction by mechanical forces, is an emerging field because neither external temperature nor pressure inputs are required. Previous studies reported enhanced catalytic activity during the mechanical treatment of supported gold catalysts for CO oxidation. So far, the processes inside the milling vessel during mechanocatalysis could not be monitored. In this work, the results of high-energy operando X-ray powder diffraction experiments and online gas analysis will be reported. A specific milling setup with a custom-made vessel and gas dosing system was developed. To prove the feasibility of the experimental setup for operando diffraction studies during mechanocatalysis, the CO oxidation with Au@Fe_2O_3 as a catalyst was selected as a well-known model reaction. The operando studies enabled monitoring morphology changes of the support as well as changes in the crystallite size of the gold catalyst. The change of the crystal size is directly correlated to changes in the active surface area and thus to the CO_2 yield. The studies confirm the successful implementation of the operando setup, and its potential to be applied to other catalytic reactions.

Introduction

Mechanochemistry has become a very vivid research field in recent years. One reason is its potential to develop processes, which are not only more cost- and energy-efficient but also environmentally friendly. In particular, the reduction or even avoidance of solvents by the direct energy transfer of the milling media to the reactants can increase the cost-efficiency as well as environmental friendliness.[1] The use of solvents and the associated recovery and purification processes are energetically costly and environmentally problematic.[1f,2] Because of these advantages, mechanochemical activation is used in the synthesis of materials for various applications, including solid-state hydrogen storage, catalysis, electrodes or electrolytes for solid batteries, fuel cell materials, or functional ceramics.[2–3] In contrast to thermally induced processes where the energy is provided globally, the energy transfer via the milling media is strictly local.[3] This local mechanical energy transfer leads to unique reaction pathways, an increase in activity, and often an alteration of selectivities compared to thermally-induced and/or solution-based reactions.[1d,f] The two most common theories to describe the mechanical activation of inorganic solids are the magma-plasma model and the hot-spot theory.[2,4] The magma-plasma model considers mostly the direct impacts of the milling media. At the collision point, temperatures above 10^4 °C can be generated, accompanied by a transient plasma and ejection of energetic species as electrons.[2,5] On the other hand, the hot-spot theory is based on the frictional processes with plastic deformations, resulting in local (~1 μm^2) temperatures above 10^3 °C for a short time (10^{-3}–10^{-4} s).[2] However, these models fail to describe the formation mechanisms of molecular organic compounds or metal-organic framework materials. For these reactions, an extensive decomposition reaction would be expected under the given conditions.[2–3] Still, some effects can be considered for all solids, such as local heating and possible eutectic melting.[3] The usage of milling media causes also rapid and efficient mixing, even of insoluble reactants, in mechanochemical processes.[1f,2] Through collision with the milling media and the resulting frictional processes, new reactive surfaces and defects are generated continuously. In addition, a crystallite size reduction and changes in the solid morphology are observed.[1a,f,3,6] These effects were successfully implemented in heterogeneous catalysis, not only for the preparation of catalytic materials but also for activation of the materials during catalysis.[1f,7] The use of mechanochemistry during a heterogeneously catalyzed reaction results in a lowering of the reaction temperature, an increase in the reactive surface area, as well as in the dispersion of a catalytically active species in a matrix, thus boosting the catalytic activity.[1f,7d–f] In one of the early

[a] Dr. H. Petersen, Dr. J. De Bellis, S. Leiting, Dr. W. Schmidt, Prof. F. Schüth, Dr. C. Weidenthaler
Max-Planck-Institut für Kohlenforschung
Heterogeneous Catalysis
Kaiser-Wilhelm-Platz 1
45470 Mülheim an der Ruhr (Germany)
E-mail: weidenthaler@mpi-muelheim.mpg.de
[b] Dr. S. M. Das
Max-Planck-Institut für Eisenforschung
Max-Planck-Straße 1
40237 Düsseldorf (Germany)

Supporting information for this article is available on the WWW under https://doi.org/10.1002/cctc.202200703

studies, Mori et al. investigated the mechanochemical methanation of CO_2 during milling NiFe- and Ru-based catalyst on a MgO support using a vibration mill.[7a] The heatable reactor was pressurized with CO_2 and H_2 at partial pressures of 100 and 500 Torr, respectively.[7a] At a reactor temperature of 180 °C, a CH_4 yield of 96% was found for a Ru-based catalyst, while under thermal catalysis conditions only a yield of 31% CH_4 was achieved.[7a] A mechanochemical pretreatment of the catalyst before the thermally driven reaction did not show any effect on the activity.[7a] The continuous generation of new catalyst surfaces, which prohibit the deactivation by deposition of carbonaceous species, was suggested to be responsible for the increased yield.[7a] A similar effect was observed for the methanation of CO via ball milling with unsupported $Co_{50}Fe_{50}$ and CoFe supported on TiO_2 as catalysts.[8] The catalytic activity under milder conditions was attributed to the generation of long-lasting and temporary defects created through the impact of the milling media.[8] Strongly increased activity was observed for CO oxidation over Pt/Al_2O_3, NiO, or Cr_2O_3 in a continuous flow reactor.[7e] A custom-made milling vessel with a gas in- and outlet was designed and used under milling with 20–50 mL min^{-1} flow of a reaction gas mixture (1% CO, 20% O_2, 79% He). The product gas was analyzed with an online-infrared (IR) spectrometer. In the case of the Cr_2O_3 catalyst, an increase in the activity by three orders of magnitude could be achieved through milling.[7e] The enhanced activity was attributed partly to transient defects in the crystal structure. In the study on the mechanochemical synthesis of supported metal catalysts (Au, Pt, Ag, Cu, Ni) on different supports (TiO_2, Al_2O_3, Co_3O_4), which was carried out under continuous flow of CO under oxidative conditions (1% CO in air, 67 mL min^{-1}), all gold-containing catalysts showed full conversion, as soon as the supported metal was sufficiently well dispersed on the support.[7d,9] Very recently, one of the most challenging heterogeneously catalyzed reactions, ammonia synthesis, was found to be possible at room temperature and atmospheric pressure over alkali metal-doped iron catalysts in a continuously operated shaker mill.[10]

In recent years, the number of in situ mechanochemical studies on the synthesis mechanism and the nature of mechanochemical activation has substantially increased.[11] Mostly, the soft matter was investigated in rather soft poly(methyl methacrylate) (PMMA) vessels.[11a–d] However, the in situ investigation of hard materials is an especially demanding task because the milling of such materials requires substantial modifications of the milling vessels concerning material hardness and the mill itself to meet the energy input requirements of the reactions. Besides, under the required high energy input, the soft PMMA decomposes, forming methyl methacrylate (MMA) and CO_2, which interfere with the monitoring of gaseous products.[11g] For in situ studies of hard materials, the inner surface of the milling vessels was made of stainless steel, and the modified vessel holders do not only place the vessel in the X-ray beam but also keep the path length of the vessel on the orbital movement more or less identical to that in the commercial milling setup as reported by Rathmann et al.[11g] Despite the growing interest, fundamental insight into the relevant processes, in particular the reasons for the enhancement of the catalytic activity in heterogeneous catalysis under milling conditions, is missing.

Inducing a catalytic reaction via mechanical forces requires neither external temperature nor pressure input. It has been demonstrated that the mechanical impact alone provides excellent catalytic performance. The constant impact provides energy input to the system and also changes particle size and shape of the catalyst. Even the surface of a catalyst may constantly change as every impact could induce structural defects extending to the particle surface. However, so far, direct characterization of the catalyst within the stainless steel milling vessels during the reaction was impossible and the catalysts could only be characterized ex-situ after the reaction. Long experience has shown that the state of a material is very often not correctly represented by ex-situ characterization before and after catalysis.[12] Taking a sample out from the catalytic reactor and exposing it to ambient conditions can lead to many reactions including re-oxidation, structural phase transformations, and morphology changes.[13] Consequently, changes of the catalyst structure, particle size, and defect concentrations cannot get related to the catalytic performance with certainty if not tracked directly by operando investigations. We therefore developed milling equipment that allows inspection of mechanocatalytic reactions directly by operando powder diffraction analysis in combination with online gas analysis. Operando mechanocatalytic studies are much more complicated than following the crystallization of soft matter in polymeric milling jars. Our studies are based on a stepwise development and testing of equipment for operando X-ray powder diffraction studies at synchrotron facilities. The setup consists of a combination of a gas dosing system with a flow-through sample cell and gas analysis. The first experiments failed because the gas flow flushed the powder from the vessel through the exhaust lines into the mass spectrometer or we faced the problem of clogging. This required several technical modifications to the gas supply before the setup worked without problems which will be described in the following sections. The major challenge of this work was to combine a mechanocatalytic reaction performed in a continuous gas stream with operando powder diffraction analysis. For this, the grinding vessels, the gas dosing system, the gas analysis, and the experimental conditions had to be designed and optimized. We chose the CO oxidation on a $Au@Fe_2O_3$ catalyst as a model reaction because it is a well-studied reaction that allows comparison of our results with those reported in literature. The objective of our study was providing prove that operando studies under milling conditions in steel jars are possible and that such studies provide valid information on the catalyst under working conditions.

To the best of our knowledge, herein we present the first operando study during milling of a mechanochemical heterogeneously catalyzed process. With the experimental setup, other heterogeneously catalyzed reactions with unknown structure-property relationships can be studied in the future.

Results and Discussion

Sample notation. The samples and measurement series are summarized in Table 1. In the series both the gas atmospheres and the sample compositions were varied. The labeling of the series will follow the notation in Table 1 hereafter.

All milling experiments (independently whether X-ray diffraction data have been collected in situ or ex-situ) have been performed with the modified milling jars shown in Figure S1. The stainless steel jars have been modified in such a way that windows are cut into the steel body which allows the incoming X-rays and the diffracted X-rays to pass the jars. The windows are covered by an X-ray transparent polymer ring which is further stabilized by a 0.5 mm thick inner stainless steel inset or a 0.5 mm thick amorphous alloy (amloy) inset. The results will show, that the choice of the window material is decisive for a comprehensive data analysis. The gas outlet was designed as a funnel, which prevents the sample from being discharged with the gas flow. The results can be grouped into three sections: (a) control experiments based on ex-situ studies of samples milled for different times under reaction conditions. From these samples, the microstructure properties of Fe_2O_3 and gold (crystal size and morphology) were determined and related to the catalytic conversion measured for the samples at different milling times. These data are the basis for comparison to estimate how meaningful and accurate the results of the operando data are. (b) operando study using a stainless steel inset for the stabilization of the X-ray transparent PMMA window, and (c) operando studies using an amorphous alloy inset for the stabilization of the PMMA window.

Table 1. Overview of the experimental conditions of all samples and measurement series.

Sample name	Composition	Sampling range	Time step	Gas atmosphere
I[a,c]	Fe_2O_3	10–60 min	10 min	static
II[a,c]	Fe_2O_3	10–60 min	10 min	CO/O_2 flow
III[a,c]	5 wt% Au + Fe_2O_3	10–60 min	10 min	CO/O_2 flow
IV[b,c]	5 wt% Au + Fe_2O_3	0-60 min	1 min	Static
V[b,c]	Fe_2O_3	0–60 min	1 min	CO/O_2 flow
VI[b,c]	5 wt% Au + Fe_2O_3	0–60 min	1 min	CO/O_2 flow
VII[b,d]	10 wt% Au + Fe_2O_3	0–60 min	1 min	CO/O_2 flow
VIII[b,d]	20 wt% Au + Fe_2O_3	0–60 min	1 min	CO/O_2 flow

[a] ex-situ series. [b] operando series. [c] inner steel inset. [d] inner amloy inset.

Ex-situ studies: Microstructure changes of the Fe_2O_3 support

For the structure refinements and morphology studies, the crystal structure data of α-Fe_2O_3 and Au were used.[11,12] In Figure 1a the XRPD data of the untreated α-Fe_2O_3 and a simulated XRPD pattern of α-Fe_2O_3 with an isotropic crystallite size (VOL_{IB}) of 9 nm are shown. α-Fe_2O_3 with isotropic crystal size has its main reflection intensity on the (104) reflection, while the main intensity in the measured data is found for the (110) reflection. The intensity ratio of these reflections reflects a different morphology of the α-Fe_2O_3-crystallites.[14] Sphere-like crystallites show an intensity ratio similar to the simulated pattern (Figure 1a). For rod- and sheet-like crystallites, this intensity ratio is inverted as observed in the measured data.[14] In addition, a significant decrease of the full width at half

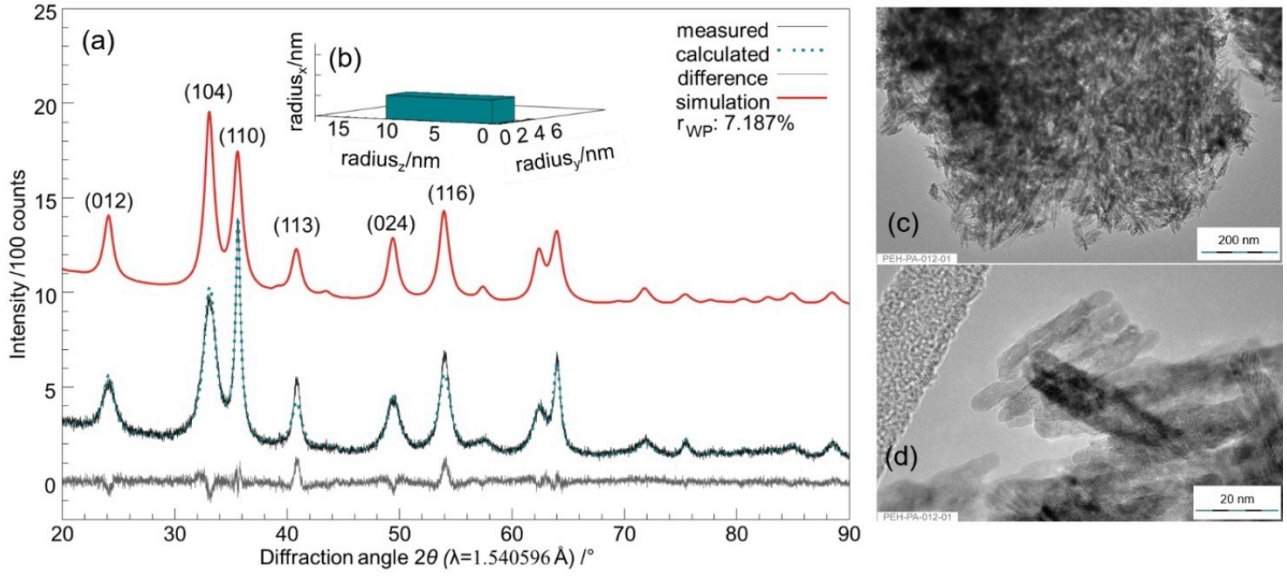

Figure 1. (a) Simulated XRPD data of α-Fe_2O_3 calculated for an isotropic crystal size (Vol_{IB}) of 9 nm (solid red line) and the Rietveld refinement of untreated, commercial α-Fe_2O_3. The measured data (solid black line) are displayed along with the calculated pattern based on an anisotropic crystallite size model (dashed green line) and the difference curve (grey). The refined anisotropic crystallite shape is shown as inset. (c + d) TEM micrographs of the untreated α-Fe_2O_3 shown in two different magnifications.

maximum (FWHM) of the (110) reflection, as compared to the (104) reflection, is observed in the measured data, implying an elongated crystallite shape along (001). Consequently, an anisotropic crystallite size with a cuboid shape with different lengths along the three axes, of which the longest runs along (001), was considered for the Rietveld analysis. For the morphology study, a macro described by Ectors et al.[15] implemented in the Rietveld program TOPAS 6 was used.[16] To simulate a cuboid crystallite shape, the crystal structure was transformed into *P*1. The Rietveld analysis results in a rod-like crystallite shape with the dimensions 10.9 nm, 3.8 nm and 2.3 nm (Figure 1 b). These findings could be confirmed via TEM micrographs where rod-like nanocrystallites are visible (Figure 1b + c). The mismatching intensities of the (113) and (116) reflections are discussed in the literature as a common feature of α-Fe_2O_3 due to disorder in the iron sublattice.[17]

In Figure 2a the ex-situ XRPD data of α-Fe_2O_3 milled for 1 h with a frequency of 25 Hz are shown. The quantification of the XRPD data reveals ~1 wt% iron as an impurity (abrasion from the steel during the milling process). In contrast to the untreated α-Fe_2O_3, the intensity ratio of the (104) and (110) reflections of the milled sample is reversed and the observed deviation of the FWHM of these reflections is no longer visible after milling. For the Rietveld analysis, an ellipsoid shape with two independent radii was supposed, resulting in an almost spherical shape with radii 8.8 nm and 11.0 nm (Figure 2 inset). The refined crystallite dimensions correspond to an increase in crystallite sizes. The spherical shape and size are confirmed by TEM micrographs (Figure 2b + c). Interestingly, the observed mismatch in the intensities of the (113) and (116) reflections, which would imply a disorder in the iron sublattice, seems to decrease upon milling. Both, the increase in the crystallite size and the ordering of the iron sublattice indicate a crystallization and structure relaxation process. Usually, mechanical treatment inflicts defects to the crystal structure and post-synthesis milling is a common method to decrease the crystallite size. Here, milling of a bulk α-Fe_2O_3 sample with a planetary mill with a sample to ball weight ratio of 1:10 and 250 rpm resulted in a decrease of the crystallite size and an increase of internal strain.[18] Prolonging the milling time caused an increase of the lattice parameters, indicating an anisotropic lattice expansion.[18]

In total, three ex-situ series were performed (Table 1): milling of Fe_2O_3 (Figure S2), Fe_2O_3 in CO/O_2 flow (Figure S3), and the mixture of 5 wt% Au and Fe_2O_3 in CO/O_2 flow (Figure 3a). The Fe_2O_3 phase shows a comparable behavior in all three milling series. After 10 min of milling, all samples have comparable intensity ratios as well as the deviation in the FWHM of the (104) and (110) reflections to the untreated α-Fe_2O_3, indicating a similar crystallite shape and size. After 30 min of milling, an increasing amount of iron impurity can be observed due to abrasion from the milling vessel and balls for all series. The quantification via Rietveld analysis shows an iron content of approximately 1–2 wt% after 60 min milling. Whereas in a closed milling vessel no formation of Fe_3O_4 could be observed (Figure S2 + S3), in CO/O_2 flow, Fe_3O_4 (Fe_3O_4: ~2 wt% sample II) could be identified after 40 min. According to previous reports, the phase transformation from α-Fe_2O_3 to Fe_3O_4 depends on the extent of iron impurity from abrasion and the partial oxygen pressure. Below an oxygen partial pressure of 77 Pa, α-Fe_2O_3 is not stable and Fe_3O_4 forms.[18a,19] The amount of iron abrasion is comparable in the three milling series, and the used CO gas mixture contains 20% oxygen which is similar to the averaged oxygen content in air. In CO atmosphere, Fe_2O_3 is reduced to Fe_3O_4.[20] In a control experi-

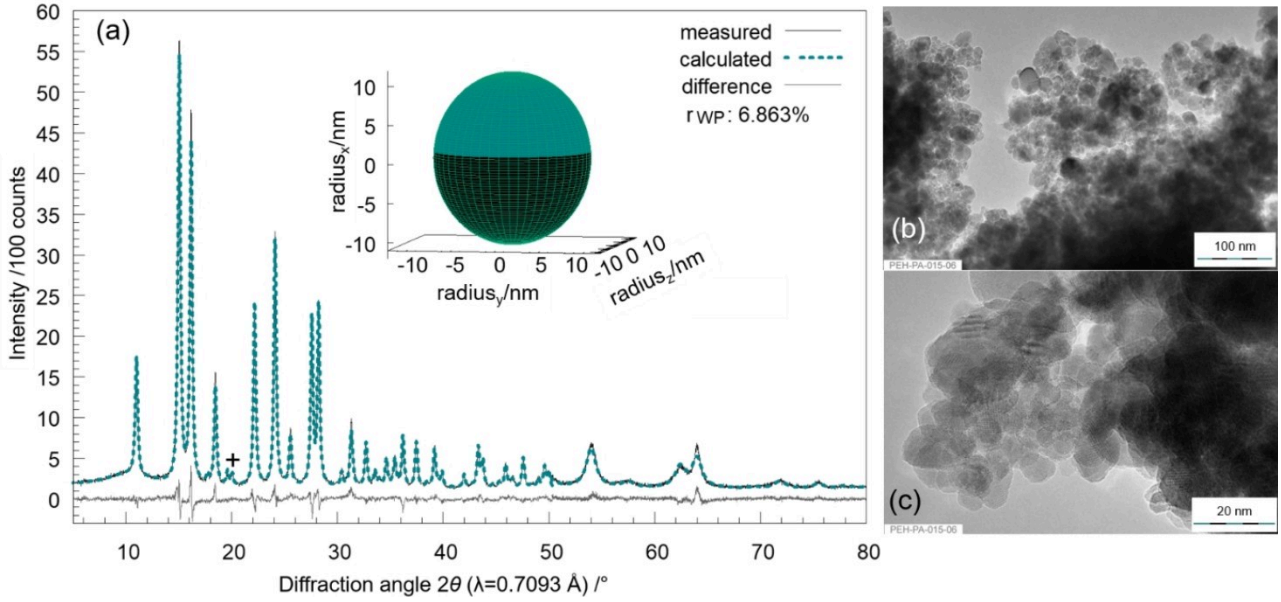

Figure 2. (a) The Rietveld refinement of ex-situ XRD data of α-Fe_2O_3 milled with 25 Hz for 1 h. The measured data (solid black line) are displayed along with the calculated pattern of the model using an anisotropic crystallite size (dashed green line) and the difference curve (grey). The refined anisotropic crystallite shape is shown as inset. The scattering contribution of iron abrasion from the milling media is marked with a cross (+) (b + c) TEM micrographs of the milled α-Fe_2O_3.

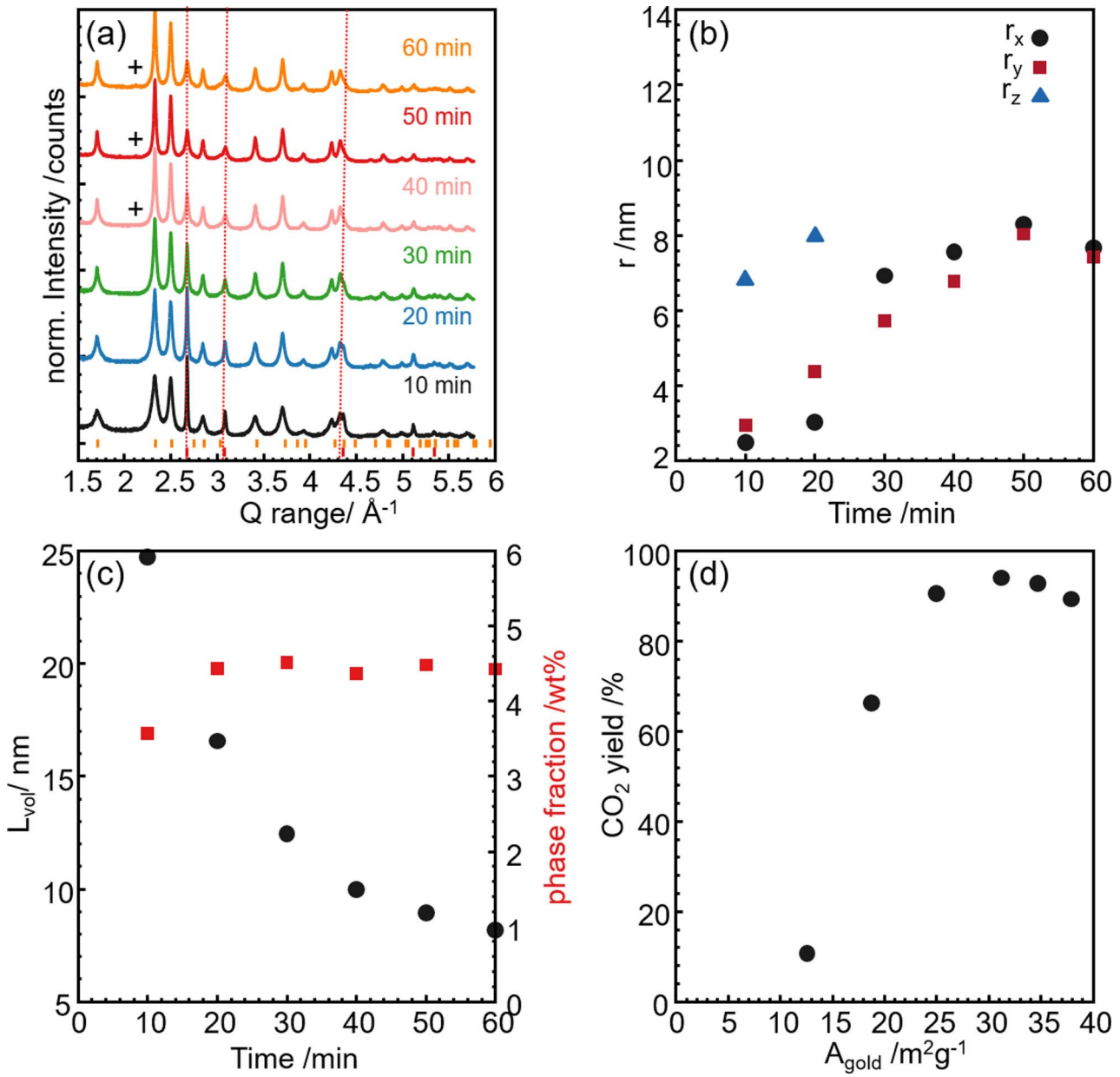

Figure 3. (a) Ex-situ XRPD data obtained from the milling of the mixture of 5 %wt gold and Fe_2O_3, the gold reflections are marked with the red dashed lines, the Fe_2O_3 reflection positions are shown by the orange tick marks. The main reflection of Fe_3O_4 is marked with a cross (+). (b) The radii of the Fe_2O_3-crystallites, and (c) the phase fraction plus the column length of the gold nanoparticles determined via Rietveld analysis. (d) The correlation between the CO_2 concentration and the surface area of the spherical gold nanocrystallites is shown in (d).

ment, Fe_2O_3 was milled in a synthetic airflow (50 mL min^{-1}). Here, also a Fe_3O_4 formation was observed (Figure S4). The Fe_3O_4 formation was observed in all flow experiments (Figure S3 + S4) but not in non-flow (static) experiments (Figure S2), indicating a relation between the Fe_3O_4 formation and the gas flow. Upon milling, the intensity ratio and FWHMs of the (104) and (110) reflections gradually change to the characteristic ratio for a spherical crystallite. The crystallite radii of α-Fe_2O_3 determined for the three milling series show comparable trends (compare Figures 3b + S2 + S3). In Figure 3b, the evolution of the Fe_2O_3 radii over milling of the mixture of 5 wt% gold and Fe_2O_3 is shown. Over the whole milling range, an increase in the radii is observed. From 10 min to 20 min of milling, a cuboid model with three independent radii results in the best fit; two radii have comparable values, while the one in the direction of (001) is significantly elongated. Milling of the sample for 30 min results in the formation of an irregular spherical crystallite with two slightly different radii. Amini et al. observed a similar behavior during the milling-induced alloying process in the Cu–Al–Mn system: the particle morphology changed from a plate-like to a semi-sphere shape with a smaller size distribution.[21] Gold catalysts with rod-shaped Fe_2O_3 support proved to be superior to spherical supports.[14a,22] Here, the morphology changed from a rod-like to a spherical shape, and

still an increase in the CO_2 yield was observed, indicating the gold phase as the major factor for the increased CO_2 yield (see Figure S5).

Ex-situ studies: Microstructure analysis of the gold nanoparticles. The evolution of the phase fraction and the crystallite diameter of the gold catalyst is shown in Figure 3c. The phase fraction scatters around 4.5 wt%, showing that a stable reaction mixture is measured. Because of the polydispersity of the gold phase, its column length distribution was determined using the whole powder pattern modeling (WPPM) approach assuming spherical crystallites with a lognormal distribution of their column length (Figure S6)[23]. The volume-weighted crystallite size (L_{Vol}) of gold can be calculated from equation 1

$$L_{Vol} = {}^{3}/_{4}e^{\mu+{}^{7}/_{2}\sigma^{2}} \quad (1)$$

with the lognormal mean μ and the variance σ. L_{Vol} of the gold nanocrystallites decreases fast from ~25 nm to ~10 nm within 40 min of milling (Figure 3c). Thereafter, the crystallite size decreases slower. The activity of gold catalysts is known to be size-dependent. High catalytic activity in CO oxidation was found specifically for gold crystallites with sizes of 0.5–3 nm.[24] Via the mechanochemical treatment of supported gold catalysts, the crystallite size of the supported active species and the active surface area can be tuned.[7d,25]

From L_{Vol}, the specific surface area of the gold catalysts (A_{gold}) was estimated with the equation 2

$$A_{gold} = \frac{6}{L_{Vol}\rho} \quad (2)$$

with the density ρ. The CO_2 yield increases strongly with an increased A_{gold} up to a value of 25 $m^2 g^{-1}$ (Figure 3d). A further increase of A_{gold} shows no benefit for the CO_2 yield. To study an additional influence of milling-induced short-lived defect sites in gold, an operando study was performed.

TEM images shown in Figure S7a–c reveal the morphology change of the Fe_2O_3 nanoparticles from rod to spherical shape being in good agreement with the XRD data (Figure 3b). Corresponding STEM-HAADF images (Figure S7d–f) illustrate the dispersion of Au during milling. Homogenous distribution of Au particles can be seen with increasing milling time. After 60 min, the particle sizes of Au are in the range of 5–10 nm which correlates well with the XRPD result.

Operando experiments: steel inset. A customized milling vessel was used for the operando measurements.[11g] To penetrate the milling jar with an X-ray beam a recess was drilled into the jar body. The opening was covered with two ring insets, an outer one made from PMMA and an inner one consisting of a 0.5 mm thick steel inset. The use of the steel inset causes the observation of typical steel reflections in addition to the reflections from the powder. The broad inner diameter of the milling vessel interferes with the diffraction geometry. As the result, four reflection sets from the steel inset can be identified (Figure S8). In addition, split iron reflections from the milling balls are observed. In comparison to the intensity of reflections of the milling media (vessel plus balls), the reflections of the milled powder are of lower intensity. Also, the diffraction patterns of the milling media and the powder are highly overlapping. As such, the main reflection of gold is strongly overlapping with a steel reflection. Together, both the low intensity of the sample reflections and the highly overlapping diffraction patterns complicate the evaluation of the XRPD data.

For the Rietveld refinements (Figure 4), the XRPD data of the empty milling vessel plus balls was subtracted from each measured XRPD data set. As a result, the measuring ranges with the main reflections of the milling media show high scattering intensities and were excluded for the refinement. Since the gold reflections are overlapping with the steel reflections of the milling media, the precision of the refinement results is limited. Therefore, the XRPD data of the gold will be discussed only qualitatively. α-Fe_2O_3 has non-overlapping reflections and can be refined with good precision. Similar to the ex-situ series, the structure of the rhombohedral hematite was transformed to *P*1 to allow for the consideration of a cuboid shape. Because of the decreased resolution, caused by the highly overlapping reflections, only two independent radii could be refined stably. The resulting crystallite radii for α-Fe_2O_3 are 5.12 nm and 2.38 nm (Figure 4b). In the operando XRPD data (Figure 5), a gradual change in the intensity ratio and the proportion of the FWHM of the (104) and (110) reflections can be observed showing morphology changes from a rod-like to a spherical crystallite.

The anisotropic crystal shape of Fe_2O_3 was refined and the resulting crystal radii are shown in Figure S9. All calculated radii show a comparable progression: first, a strong increase up to 30 min of milling, followed by a plateau (Figure S9a + b). Here, the determined radii of each sample show comparable values indicating the formation of spherical crystallite shapes. In general, the shorter radii show a stronger increase. The main gold reflection highly overlaps with the steel reflection (Figure S10, marked area). Upon milling the gold reflection seems

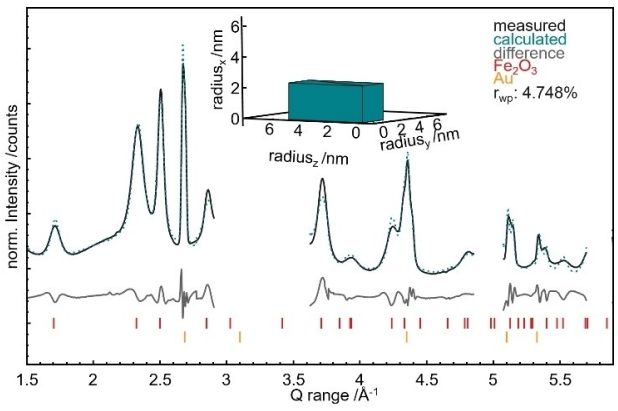

Figure 4. Rietveld refinement of operando XRPD data of 5 wt% Au + Fe_2O_3 milled for 1 min. The measured data are displayed in black, the calculated pattern in green, and the difference curve in grey. The positions of the reflection sets of α-Fe_2O_3 (red, top row) and gold (orange, bottom row) are marked by colored bars. The refined anisotropic crystallite shape is shown as inset.

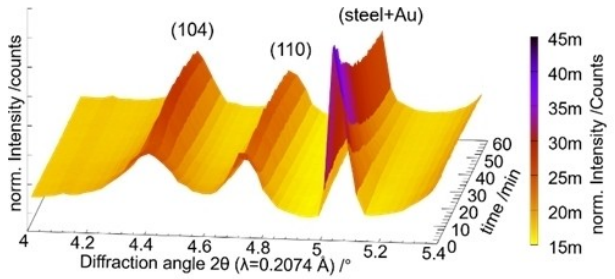

Figure 5. Normalized operando XRPD data of 5 wt% Au + Fe_2O_3 milled for 1 h. The observed Fe_2O_3 reflections are labeled with their indices.

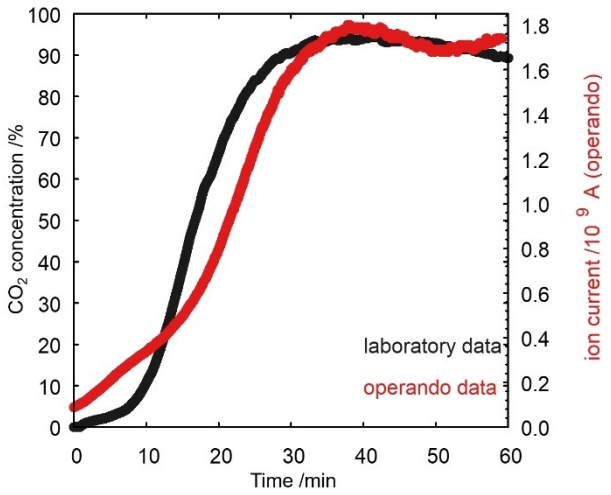

Figure 6. Comparison of the CO_2 concentration obtained from the laboratory experiment (black) and and the monitored ion current of the $m_i = 44$ u from the operando experiment (red). For both experiments a 5wt%Au@Fe_2O_3 catalyst was milled in a gas (1% CO, 20% O_2, 79% He) flow of 50 mL min^{-1}.

to decrease and broaden, showing either that the gold might stick to the vessel walls and thus be undetectable by XRPD, or the gradual decrease of the crystallite size of gold. The samples from the operando milling experiments were recovered and analyzed via XRPD after the experiment. The sample with 5 wt% gold shows a log mean of column length distribution of 2.5(2) nm ($L_{Vol} = 9$ nm) after the operando experiment, clearly proving the reduction of the crystallite size. The original mass spectrometry (MS) data of the measurement series V and VI are shown in Figure S11. To determine the blind activity of the milling setup, 1 g of poorly active Fe_2O_3 was milled under CO flow. The modified vessel design with the insets prohibits successfully the decomposition of the PMMA inset and as such the release of decomposition products into the effluent gas stream.[11g] The blank measurement shows a minor amount of CO_2 in the gas atmosphere after 10 min. A significantly higher CO_2 concentration as compared to the blank curve is observed with 5 wt% Au (VI) on iron oxide. The CO_2 signal of the measurement serie VI shows the start of the catalytic oxidation of CO to CO_2 after ~5 min of milling. After 10 min of milling, a strong increase in the CO_2 concentration is observed. The catalyst reaches a plateau of activity after 30 min. In Figure 6, the obtained CO_2 concentration determined in the laboratory setup is shown together with the CO_2 signal measured in the operando experiment. The values obtained during the operando measurement can not be quantified since neither an internal standard was used nor calibration of the MS was performed. Nevertheless, the comparable slopes of the data series obtained in the operando and laboratory setup show a comparable evolution, proving a successful implementation of the gas atmosphere analysis in the experiment.

Operando experiments: amloy inset. As described above, the use of an inner steel inset resulted in strong scattering contributions of steel, overlapping with the gold reflections. To reduce the scattering intensity of steel, the steel inset was exchanged for a custom-made amorphous alloy (amloy) inset. In total, two operando series (VII and VIII) were conducted (compare Table 1). In the XRPD data using the amloy inset, three broad scattering features from the amloy can be observed (Figure S12). These scattering features overlap with the main reflection of the α-Fe_2O_3 affecting the accuracy of the individual crystallite radii perpendicular and along the growth direction (Figure S13). However, the determined radii of the experimental series VII–VIII show a comparable behavior to the series with the steel inset (series V–VI; Figure S9). Both, the change of a rod-like α-Fe_2O_3 with two individual crystal radii to a spherical morphology with one radius as well as the constant increase of radii upon milling can be monitored. In addition, the scattering contribution of steel is significantly reduced (compare Figure S8 and Figure S12). As a result, particularly the main reflections of gold are now sufficiently resolved to perform structural investigations. The microstructural analysis of the gold upon milling was performed via the WPPM approach. From the derived column length distributions, the average surface area of the gold was calculated, similarly to the in detail described procedure for the ex-situ serie III. The obtained gold surface area from the operando series (VII: 10 wt%Au@Fe_2O_3 and VIII: 20 wt%Au@Fe_2O_3) are in good agreement with the results from the ex-situ experiments with the mixture 5 wt%Au@Fe_2O_3, validating the method (Figure 7).

Summary

Commercial Fe_2O_3 has a rod-like crystallite shape. The anisotropic crystallite size refinement results in two short dimensions (2.3 nm, 3.8 nm) and an elongated one along the (001) direction. Upon milling, the morphology of the Fe_2O_3 is gradually changing to a spherical shape. The analysis of the operando XRPD data shows major changes in the first 30 min. After milling for 30 min, the determined crystal dimensions of Fe_2O_3 are similar, indicating a spherical shape. Interestingly, also the CO_2 concentration of the catalyst loaded with 5 wt% Au reaches a maximum at 30–40 min. However, studies of the influence of morphology of the Fe_2O_3 support on CO oxidation activity of gold supported on iron oxide showed that a rod-like shape is superior to a spherical shape.[22,26] Thus, in our case, the reason for the increase in CO_2 concentration must be related to

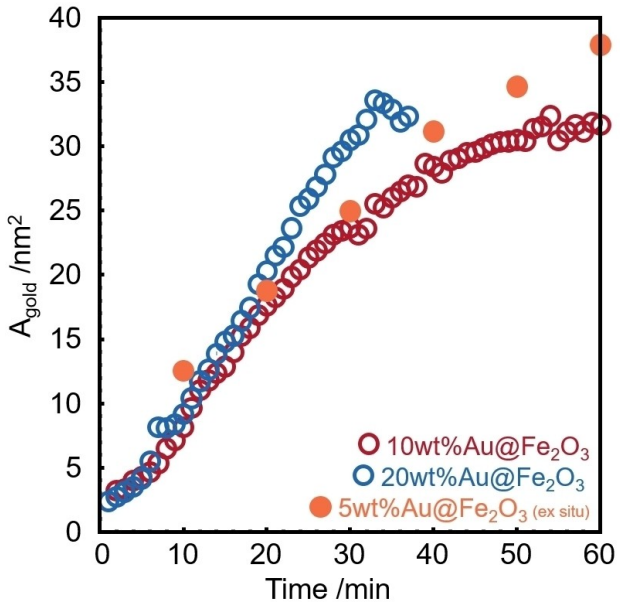

Figure 7. Evolution of the gold surfaces of Au@Fe_2O_3-samples with different Au concentrations obtained from operando milling experiments. The milling vessel was equipped with an amorphous amloy inset. For comparison the results from the ex-situ experiment milling 5 wt%@Fe_2O_3 are included.

the gold. The determined phase fraction of gold is unchanged, showing that a stable mixture is achieved. In the first 40 min, a decrease in the crystallite size of gold from 16 nm to 3 nm is observed. The CO_2 concentration increases strongly with the increase of the specific gold surface area from 10 to 25 $m^2 g^{-1}$ calculated from the size distribution obtained for gold. For a further increase of the gold surface, no beneficial effect could be observed. The comparability of the MS data obtained in the laboratory and the operando setup proves the successful modification of the milling setup, allowing to monitor the solid catalyst during CO oxidation in a ball mill. In particular, the new vessel design protects the PMMA inset from decomposition. Substitution of the window material with similar mechanical properties but lower scattering intensity will be advantageous for further studies. In particular, to investigate the postulated short-lived defects possible in the active gold phase induced by collisions with the milling media, a substitution of the steel inset is inevitable. With this work, we demonstrate that it is possible to follow catalytic reactions within a ball-mill by operando high-energy X-ray diffraction experiments coupled with online gas analysis. So far, mechanocatalysis was kind of a 'black-box' with respect to in situ changes of the crystalline catalysts. The successful modification of the milling setup and the combination of XRD and online gas analysis opens the option to monitor also complex catalytic reactions proceeding in a ball-mill. With the modification of the milling setup, it was possible for the first time to monitor how catalysts change during a mechanocatalytic reaction. The combination of high-energy X-ray diffraction and gas analysis enables a direct correlation between catalytic activity and changes in the microstructure and atomic structure of catalysts. The comparison of ex-situ diffraction data with the operando data confirmed that the experimental setup is suitable to perform operando mechanocatalytic experiments at synchrotron sources. Such types of experiments enable the monitoring of structural changes and correlate them directly to the catalytic performance of a solid catalyst. The methodology we report can be adapted to other reactions, as gas flow, catalyst composition, and online gas analysis can be easily changed. This opens the door widely for future experiments on mechanochemical and mechanocatalytic reactions with hard solids that can now be studied under working conditions in various gas atmospheres and gas flows. We think that these prospects are of great interest to readers working in the field of mechanochemistry.

Experimental Section

Milling-setup. All mechanical experiments were conducted with a RETSCH MM400 shaker mill (Retsch GmbH Haan, Germany). The mill was equipped with modified holders to place the reaction vessel in the X-ray beam on the diffraction setup on a synchrotron beamline. The customized holders are designed to prohibit a decrease in kinetic energy caused by geometrical changes in the shaker mill.[11g] To enable the X-ray beam to penetrate through the stainless steel vessel (V = 25 mL) has been modified as described by Rathmann et al. (Figure S1a).[11g] Two cutouts in the steel body were covered with insets, the outer inset is made from poly(methylmethacrylate) (PMMA). Two types of inner insets for the stabilization of PMMA were tested: a 0.5 mm thick steel inset and a custom-made and an amorphous amloy inset (Heraeus Holding GmbH, Deutschland), respectively (Figure S1b). The amloy consists of 24 wt% Cu, 4 wt% Al, 2 wt%, and Zr for the balance. In addition, in- and outlet lines on the opposite ends of the vessel allowed for a constant gas flow through the vessel (see Figure S1a). A funnel with a frit was connected to the outlet to create turbulence in the gas stream and prohibit the accumulation of powder in the gas line. For all milling experiments, 1 g of powder containing α-Fe_2O_3 (Alfa Aesar; CAS: 1309-37-1) and 0 wt%, 5 wt%, 10 wt% or 20 wt% Au (Alfa Aesar; CAS: 7440-57-5)) was loaded into the milling vessel. Two 15 mm steel balls (m_{ball} = 13–14 g) were used for each experiment. All experiments were carried out with a frequency of 25 Hz. For the CO oxidation experiments, a gas mixture with 1% CO, 20% O_2, 79% He was passed with a flow of 50 mL min^{-1} through the vessel. In the ex-situ experiments, the setup was flushed with He before each experiment. Then, the reaction gas was passed through the milling jar. The flow was regulated via mass flow controllers (MFCs) calibrated with a DryCalPro gas calibrator (Mesalabs). The gas composition downstream from the milling capsule was continuously analyzed using a non-dispersive IR spectrometer ABB EL 300 series with a URAS 26 calibrated up to a CO or CO_2 concentration of about 2%. The data were analyzed using the computer program LabVIEW RunTime (made in-house). The experiments were initiated only after reaching stable CO values. During each experiment, the gas flow was periodically checked via a bubble meter to ensure continuous flow was maintained. For the operando measurement series, a ThermoStar mass spectrometer equipped with a QME 200 analyzer (Pfeiffer Vacuum GmbH, Aßlar, Germany) was connected via a steel capillary to the gas outlet of the vessel to analyze the gas atmosphere. Since no internal standard was used during the recording of the MS data, the MS data can not be quantified.

X-ray powder diffraction (XRPD). XRPD patterns of the obtained samples were collected with a Rigaku SmartLab diffractometer (Tokyo, Japan) equipped with a 9 kW rotating anode using $CuK_{\alpha 1}$

radiation (λ = 1.540596 Å), a primary focusing optic (Johansson monochromator), an incident slit 1/3° and a 5 mm mask. All XRPD measurements were measured with 1°/min using the XRF-mode to suppress fluorescence. The operando experiments were conducted at beamline P02.1 (Petra III DESY, Hamburg, Germany) using the experimental setup as described above. The XRPD data were collected with a Varex XRD 4343CT (150 × 150 μm² pixel size, 2880 × 2880 pixel area) detector. For the data collection, a wavelength of λ = 0.20741 Å was used. Each XRPD pattern was recorded with 60 s per frame. For the data integration, Dawn 2.6.0 (Diamond Light Source Ltd, Oxfordshire, United Kingdom) was used.[27] The evaluation of the XRPD data was performed with TOPAS 6 (Bruker AXS GmbH, Karlsruhe, Germany).[16] The implemented fundamental parameter approach was used to describe the profile of the diffractometer; it was determined using a Si (NIST 640e) standard reference material. The anisotropic crystallite sizes were determined using the macro described by Ectors et al.[15] The size of the gold nanoparticles was evaluated with the whole powder pattern modeling approach implemented in TOPAS 6.[23b–d,28]

High-Resolution Transmission Electron Microscopy (HR-TEM). The HR-TEM micrographs were recorded with a Hitachi HF2000 TEM instrument equipped with a cold field-emission gun (FEG) and operated with 200 keV acceleration voltage. The specimens for TEM measurement were prepared and deposited on a Cu lacey-carbon grid. High angle annular dark field images in scanning transmission electron microscopy mode were acquired in JEOL JEM 2200FS microscope operating at 200 keV voltage.

Acknowledgements

We acknowledge DESY (Hamburg, Germany) a member of the Helmholtz Association HGF, for the provision of experimental facilities. Parts of this research were carried out at PETRA III, beamline P02.1 and we would like to thank M. Etter for technical support. We thank P. Sharma, I. Kappel, T. Rathmann, J. Ternieden, F. Winkelmann and S. Reichle (MPI) for support during beamtime and J. Ternieden for the in-house XRD measurements. E. Budiyanto (MPI) is acknowledged for the TEM analysis, the precision mechanics workshop and especially W. Kersten for the work on the modified milling vessels. Open Access funding enabled and organized by Projekt DEAL.

Conflict of Interest

The authors declare no conflict of interest.

Keywords: Anisotropic crystallite size · CO oxidation · Mechanochemistry · Operando analysis · Supported catalysts

[1] a) P. Baláž, A. Aláčová, M. Achimovičová, J. Ficeriová, E. Godočíková, *Hydrometallurgy* **2005**, *77*, 9–17; b) I. S. Ahn, S. Y. Bae, H. J. Cho, C. J. Kim, D. K. Park, *Prog. Powder Metall.* **2007**, *534–536*, 225–228; c) Z. Bujňáková, E. Dutková, M. Kello, J. Mojžiš, M. Baláž, P. Baláž, O. Shpotyuk, *Nanoscale Res. Lett.* **2017**, *12*, 328; d) J. M. Andersen, J. Mack, *Chem. Sci.* **2017**, *8*, 5447–5453; e) P. Baláž, E. Dutková, *Miner. Eng.* **2009**, *22*, 681–694; f) C. Bolm, J. G. Hernandez, *Angew. Chem. Int. Ed.* **2019**, *58*, 3285–3299; *Angew. Chem.* **2019**, *131*, 3320–3335.

[2] S. L. James, C. J. Adams, C. Bolm, D. Braga, P. Collier, T. Friščić, F. Grepioni, K. D. M. Harris, G. Hyett, W. Jones, A. Krebs, J. Mack, L. Maini, A. G. Orpen, I. P. Parkin, W. C. Shearouse, J. W. Steed, D. C. Waddell, *Chem. Soc. Rev.* **2012**, *41*, 413–447.

[3] E. Boldyreva, *Chem. Soc. Rev.* **2013**, *42*, 7719–7738.

[4] F. Delogu, G. Mulas, in *High-Energy Ball Milling* (Ed.: M. Sopicka-Lizer), Woodhead Publishing, **2010**, pp. 92–110.

[5] P. G. Fox, *J. Mater. Sci.* **1975**, *10*, 340–360.

[6] Q. Zhang, F. Saito, *Adv. Powder Technol.* **2012**, *23*, 523–531.

[7] a) S. Mori, W. C. Xu, T. Ishidzuki, N. Ogasawara, J. Imai, K. Kobayashi, *Appl. Catal. A* **1996**, *137*, 255–268; b) G. Mulas, L. Schiffini, G. Cocco, *J. Mater. Res.* **2004**, *19*, 3279–3289; c) R. Eckert, M. Felderhoff, F. Schüth, *Angew. Chem. Int. Ed.* **2017**, *56*, 2445–2448; *Angew. Chem.* **2017**, *129*, 2485–2488; d) H. Schreyer, R. Eckert, S. Immohr, J. de Bellis, M. Felderhoff, F. Schüth, *Angew. Chem. Int. Ed.* **2019**, *58*, 11262–11265; *Angew. Chem.* **2019**, *131*, 11384–11387; e) S. Immohr, M. Felderhoff, C. Weidenthaler, F. Schüth, *Angew. Chem. Int. Ed.* **2013**, *52*, 12688–12691; *Angew. Chem.* **2013**, *125*, 12920–12923; f) A. P. Amrute, J. De Bellis, M. Felderhoff, F. Schüth, *Chem. Eur. J.* **2021**, *27*, 6819–6847.

[8] G. Mulas, R. Campesi, S. Garroni, F. Delogu, C. Milanese, *Appl. Surf. Sci.* **2011**, *257*, 8165–8170.

[9] H. Schreyer, doctoral thesis thesis, Ruhr-Universität Bochum (Bochum), **2018**.

[10] S. Reichle, M. Felderhoff, F. Schüth, *Angew. Chem. Int. Ed.* **2021**, *60*, 26385–26389.

[11] a) T. Friščić, I. Halasz, P. J. Beldon, A. M. Belenguer, F. Adams, S. A. J. Kimber, V. Honkimäki, R. E. Dinnebier, *Nat. Chem.* **2013**, *5*, 66–73; b) D. Gracin, V. Štrukil, T. Friščić, I. Halasz, K. Užarević, *Angew. Chem. Int. Ed.* **2014**, *53*, 6193–6197; *Angew. Chem.* **2014**, *126*, 6307–6311; c) L. Batzdorf, F. Fischer, M. Wilke, K.-J. Wenzel, F. Emmerling, *Angew. Chem.* **2015**, *54*, 1799–1802; d) J.-L. Do, T. Friščić, *ACS Cent. Sci.* **2017**, *3*, 13–19; e) T. Friščić, C. Mottillo, H. M. Titi, *Angew. Chem. Int. Ed.* **2020**, *59*, 1018–1029; *Angew. Chem.* **2020**, *132*, 1030–1041; f) H. Petersen, S. Reichle, S. Leiting, P. Losch, W. Kersten, T. Rathmann, J. Tseng, M. Etter, W. Schmidt, C. Weidenthaler, *Chem. Eur. J.* **2021**, *27*, 12558–12565; g) T. Rathmann, H. Petersen, S. Reichle, W. Schmidt, A. P. Amrute, M. Etter, C. Weidenthaler, *Rev. Sci. Instrum.* **2021**, *92*, 114102.

[12] a) J.-D. Grunwaldt, B. S. Clausen, *Top. Catal.* **2002**, *18*, 37–43; b) E. Stavitski in *In-situ characterization of heterogeneous catalyst* (Eds.: J. A. Rodriguez, J. C. Hanson, P. J. Chupas), John Wiley & Sons, Ltd, **2013**, pp. 241–265; c) A. M. Beale, E. Stavitski, B. M. Weckhuysen, *Encyclopedia of life support systems (EOLSS)* **2015**.

[13] C. Weidenthaler in *Crystallography in Materials Science: From Structure-Property Relationships to Engineering* (Eds. S. Schorr, C. Weidenthaler) De Gruyter, **2021** pp 1–54.

[14] a) J. R. Jesus, R. J. S. Lima, K. O. Moura, J. G. S. Duque, C. T. Meneses, *Ceram. Int.* **2018**, *44*, 3585–3589; b) C. D. Powell, A. W. Lounsbury, Z. S. Fishman, C. L. Coonrod, M. J. Gallagher, D. Villagran, J. B. Zimmerman, L. D. Pfefferle, M. S. Wong, *Nano Convergence* **2021**, *8*, 8.

[15] D. Ectors, F. Goetz-Neunhoeffer, J. Neubauer, *Powder Diffr.* **2017**, *32*, 27–34.

[16] A. Coelho, *J. Appl. Crystallogr.* **2018**, *51*, 210–218.

[17] I. V. Chernyshova, M. F. Hochella Jr, A. S. Madden, *Phys. Chem. Chem. Phys.* **2007**, *9*, 1736–1750.

[18] a) O. M. Lemine, *Superlattices Microstruct.* **2009**, *45*, 576–582; b) O. M. Lemine, M. Sajieddine, M. Bououdina, R. Msalam, S. Mufti, A. Alyamani, *J. Alloys Compd.* **2010**, *502*, 279–282.

[19] a) T. Kosmac, T. H. Courtney, *J. Mater. Res.* **1992**, *7*, 1519–1525; b) M. Zdujić, Č. Jovalekić, L. Karanović, M. Mitrić, *Mater. Sci. Eng. A* **1999**, *262*, 204–213.

[20] Y. D. Wang, X. N. Hua, C. C. Zhao, T. T. Fu, W. Li, W. Wang, *Int. J. Hydrogen Energy* **2017**, *42*, 5667–5675.

[21] R. Amini, S. M. M. Mousavizad, H. Abdollahpour, M. Ghaffari, M. Alizadeh, A. K. Okyay, *Adv. Powder Technol.* **2013**, *24*, 1048–1053.

[22] a) Y. Gao, F.-K. Chiang, S. Li, L. Zhang, P. Wang, E. J. M. Hensen, *Chin. J. Catal.* **2021**, *42*, 658–665; b) L. Sun, W. Zhan, Y.-A. Li, F. Wang, X. Zhang, X. Han, *Inorg. Chem. Front.* **2018**, *5*, 2332–2339.

[23] a) P. Scardi, M. Leoni, *Acta Crystallogr. Sect. A* **2001**, *57*, 604–613; b) P. Scardi, *Z. Kristallogr.* **2002**, *217*, 420–421; c) P. Scardi, M. Leoni, *J. Appl. Crystallogr.* **2006**, *39*, 24–31; d) P. Scardi, M. Ortolani, M. Leoni, *Mater. Sci. Forum* **2010**, *651*, 155–171; e) P. Scardi, C. L. Azanza Ricardo, C. Perez-Demydenko, A. A. Coelho, *J. Appl. Crystallogr.* **2018**, *51*, 1752–1765.

[24] a) I. Laoufi, M. C. Saint-Lager, R. Lazzari, J. Jupille, O. Robach, S. Garaudée, G. Cabailh, P. Dolle, H. Cruguel, A. Bailly, *J. Phys. Chem. C* **2011**, *115*, 4673–4679; b) I. N. Remediakis, N. Lopez, J. K. Nørskov, *Appl. Catal. A* **2005**, *291*, 13–20; c) Y. Liu, C.-J. Jia, J. Yamasaki, O. Terasaki, F.

Schüth, *Angew. Chem.* **2010**, *122*, 5907–5911; *Angew. Chem. Int. Ed.* **2010**, *49*, 5771–5775; d) A. Herzing Andrew, J. Kiely Christopher, F. Carley Albert, P. Landon, J. Hutchings Graham, *Science* **2008**, *321*, 1331–1335.
[25] J. De Bellis, M. Felderhoff, F. Schüth, *Chem. Mater.* **2021**, *33*, 2037–2045.
[26] L. P. Salamakha, E. Bauer, S. I. Mudryi, A. P. Goncalves, M. Almeida, H. Noel, *J. Alloys Compd.* **2009**, *479*, 184–188.
[27] J. Filik, A. W. Ashton, P. C. Y. Chang, P. A. Chater, S. J. Day, M. Drakopoulos, M. W. Gerring, M. L. Hart, O. V. Magdysyuk, S. Michalik, A. Smith, C. C. Tang, N. J. Terrill, M. T. Wharmby, H. Wilhelm, *J. Appl. Crystallogr.* **2017**, *50*, 959–966.
[28] L. Rebuffi, A. Troian, R. Ciancio, E. Carlino, A. Amimi, A. Leonardi, P. Scardi, *Sci. Rep.* **2016**, *6*, 20712.

Manuscript received: June 1, 2022
Revised manuscript received: August 15, 2022
Accepted manuscript online: August 15, 2022
Version of record online: September 9, 2022